JAPANESE JOURNAL OF APPLIED PHYSICS
VOL. 27, NO. 7, JULY, 1988, pp. 1299-1303

Analytical Liner Current Distribution and Magnetic Field near Port Section with Circular and Elliptical Shapes

Shunjiro SHINOHARA

Department of Physics, Faculty of Science, University of Tokyo, Bunkyo-ku, Tokyo 113

(Received March 9, 1987; revised manuscript received November 2, 1987; accepted for publication May 28, 1988)

Liner current and electric field distributions are analytically solved, and an induced error magnetic field is numerically calculated near the port section with circular and elliptical shapes using plane geometry. The effect of an elongation ratio of the port cross section and e-folding length of the magnetic field are also studied.

KEYWORDS: RFP, liner current, electric field, port section, error field

§1. Introduction

Recently, Reversed Field Pinch (RFP)[1] devices have produced experimental results indicating a favorable increase in plasma parameters with an increase in the plasma current.[2-8] However, the field errors degrade the plasma and must be minimized in order to get better plasma performance.[3,9] The error fields can be generated by the effects of the liner, shell, current feeder, supports of a vessel, iron core, toroidal field ripple, inaccurate positioning of coils, etc.

Here, we calculate the liner current in the port section, which is inevitably used for diagnostics, analytically, and discuss it from a viewpoint of the error fields; the liner current flows with the direction of the applied electric field and takes a winding path to avoid a port hole, which makes the error fields.

Section 2 deals with the analytical solution of the complex electrostatic potential near the port with circular and elliptical shapes. The liner current and electric field distributions are discussed in §3. Numerical analyses of the error magnetic field distributions are performed in §4. Finally, the conclusion is presented in §5.

§2. Analytical Solution of Complex Electrostatic Potential

For simplicity, we assume a plane geometry of the liner instead of a cylindrical one, and the circular and elliptical cross sections of the port are used. Then, the analytic solution of the complex electrostatic potential, and thus the electrostatic potential, electric field and liner current distributions, can be derived from the analogy of the fluid mechanics with a two-dimensional geometry without the vorticity and compressibility.

In the presence of a circular cylinder, the solution (outside of the circle) of the uniform flow is

$$f=U(Z+R^2/Z), \tag{1}$$

where $f=\Phi+i\Psi$ (Φ: velocity potential, Ψ: stream function) is a complex velocity potential, U is a constant flow velocity, $Z=x+iy$ is a two-dimensional position and R is the radius of the cylinder. Here, we can use the Cauchy-Riemann relation from the harmonic function of $f(\Delta\Phi=\Delta\Psi=0)$.

The complex velocity potential f, stream flux function Ψ, velocity potential Φ, velocity ($=\nabla\Phi$) and constant velocity U correspond to the the complex electrostatic potential, electric flux function, electrostatic potential ϕ, electric field $-E$ and constant applied electric field $-E_0$ (x direction), respectively, under a steadystate condition; $\Delta\phi=0$ on the liner as $\nabla\cdot E=0$ and $E=-\nabla\phi$ (ϕ: electrostatic potential). Here, the current density j is expressed as E/η (η: resistivity) on the liner as long as no electromotive force such as $v\times B$ and $\partial B/\partial t$ is present. The boundary condition is that the normal components, j_n and also $E_n=\eta j_n$, are zero on the liner side of the circle (liner-hole interface), which satisfies eq. (1).

In the hole (vacuum) region ($E\neq 0$ and $j=0$),

$$f=2UZ, \tag{2}$$

is derived from $\Delta\Phi=\Delta\Psi=0$ and a continuity condition of the tangential electric field at the inner and outer side surfaces of the circle. Note that $\nabla\Psi(\Psi)$ falls at right angles with $\nabla\Phi(\Phi)$ and both Ψ and Φ are single-valued functions on the whole region.

Next, an elliptical cross section of the port is considered. Utilizing the Joukowski transformation of

$$Z=\zeta+a^2/\zeta, \tag{3}$$

($a=$constant$<R$) and flow angle α with respect to the horizontal axis of x, we have the following equation on the liner.

$$f=U(e^{-i\alpha}\zeta+R^2e^{i\alpha}/\zeta). \tag{4}$$

Inside the hole, the same procedure with the circular port leads to the following equation.

$$f=2Ue^{-i\alpha}\frac{Z-i(a/R)^2\bar{Z}}{1-(a/R)^4}. \tag{5}$$

Here, $\bar{Z}$ is a complex conjugate of Z. Equations (4) and (5) reduce to eqs. (1) and (2), respectively, for the case of $a=0$ as it is evident from eq. (3). The elongation of the ellipse, defined as the ratio of major to minor semiaxis lengths, is $\kappa=(R^2+a^2)/(R^2-a^2)(\geq 1)$.

Using eqs. (1)-(5), the current density profile on the liner and the electric field on the whole region can be derived in the presence of the constant electric field E_0. Here, free parameters to determine the solution are a, R,

α and U. Note that values of Ψ and E_n are not continuous across the boundary (liner-hole interface), although Φ value is continuous.

§3. Liner Current and Electric Field Distributions

First, the circular cross section of the port is considered by the use of eqs. (1) and (2). Figure 1(a) shows the contours of the flux function Ψ, which shows the electric field and current flowing (on the liner) directions, when the constant electric field E_0 (x direction) is applied. Here, the Ψ value on the circular surface is different from that on any contour lines in the hole region except for the x axis. In this calculation, mesh sizes in both x and y directions are 70 for $|x|, |y| \leq 3$ with a port radius of 1. In Fig. 1(b), the contours of the potential Φ are shown. The electric field $E = -\nabla\phi$ becomes smaller near the circular surface of $y=0$, and is constant with $2E_0$ (x direction) in the hole region due to the presence of the surface electric charge. Figure 1(c) shows the contours of the normalized current density $|j/j_0|$, where j_0 is a constant value at the infinite distance away from the port. The distortion of the current density distribution near the port is evident; $\nabla\Psi$ at the top and bottom sides of the port is large, but small near the right and left sides. The value of $|j/j_0|$ has the maximum value of 2 at the top and bottom tips of the port and zero at the port surface on the midplane.

Next, the elliptical shape of the port with an elongation ratio κ of 2.7 is considered by the use of eqs. (3)-(5). Here, this shape is similar to the side port, 19 cm high and 7 cm wide, in the REPUTE-1 device.[7,10,11] Figures 2(a), 2(b) and 2(c) show the contours of Ψ, Φ and $|j/j_0|$, respectively, with the constant electric field E_0 (x direction), which is parallel to the minor axis of the ellipse. It also can be found that $|j/j_0|$ has the maximum of $1+\kappa=3.7$ at the top and bottom tips of the port. Inside the hole, the electric field (x direction) is constant of $(1+\kappa)E_0=3.7E_0$.

Contrary to the Fig. 2 case, the current disturbance and the maximum current density are smaller when the electric field is along the major axis of the ellipse (x direction), as is shown in Fig. 3; the maximum value of $|j/j_0|$ at the top and bottom sides of the port is $1+(1/\kappa) = 1.37$. (Inside the hole, the electric field (x direction) has a constant value of $\{1+(1/\kappa)\}E_0=1.37E_0$.) Therefore, the current distortion is larger when the electric field is applied along the minor axis of the ellipse than that along the major axis. In any case, the disturbed region of the current density extends to an order of one port size in both the x and y directions ($|j/j_0|$ is ~ 1 at the outer region). Due to this fact, the liner current distribution in the port section is not affected by the presence of the neighboring port section in the REPUTE-1, because the toroidal distance between the port sections is 36 cm, which is larger than the port size by more than twice.

In Fig. 4, the dependence of the normalized maximum current density on the liner and electric field in the hole region on the elongation of the port cross section is

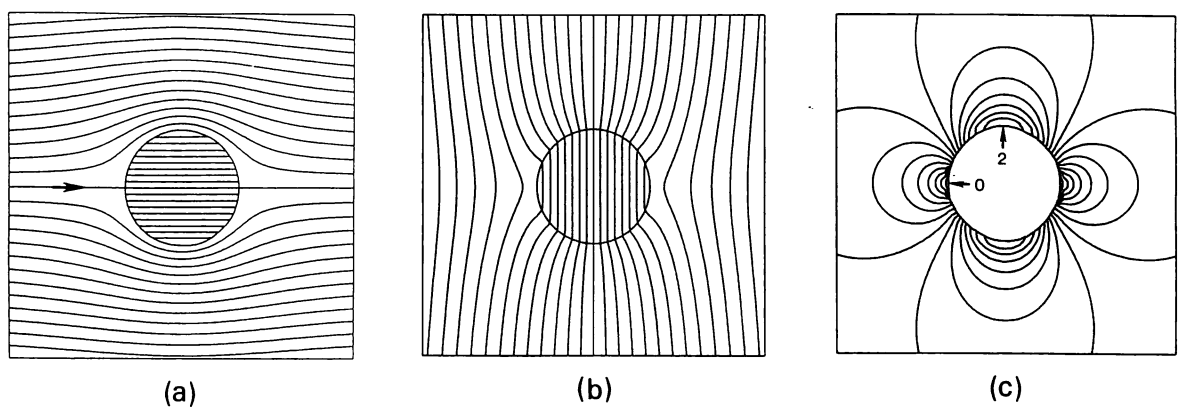

Fig. 1. Contours of flux function Ψ (a), potential Φ (b) and normalized current density $|j/j_0|$ (c) with a circular shape of the port in the presence of constant electric field (arrow) in x direction.

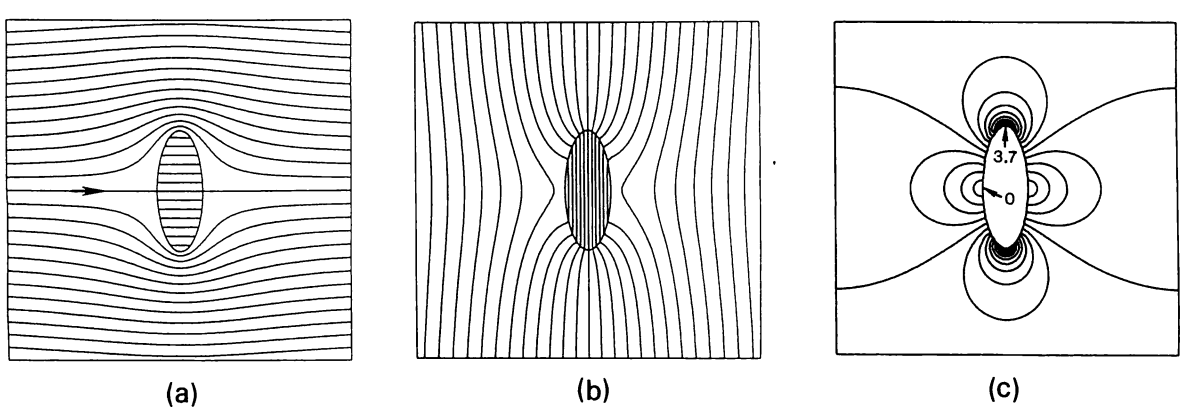

Fig. 2. Contours of flux function Ψ (a), potential Φ (b) and normalized current density $|j/j_0|$ (c) with an elliptical shape of the port (elongation ratio κ is 2.7) in the presence of constant electric field (arrow) in x direction (parallel to minor axis).

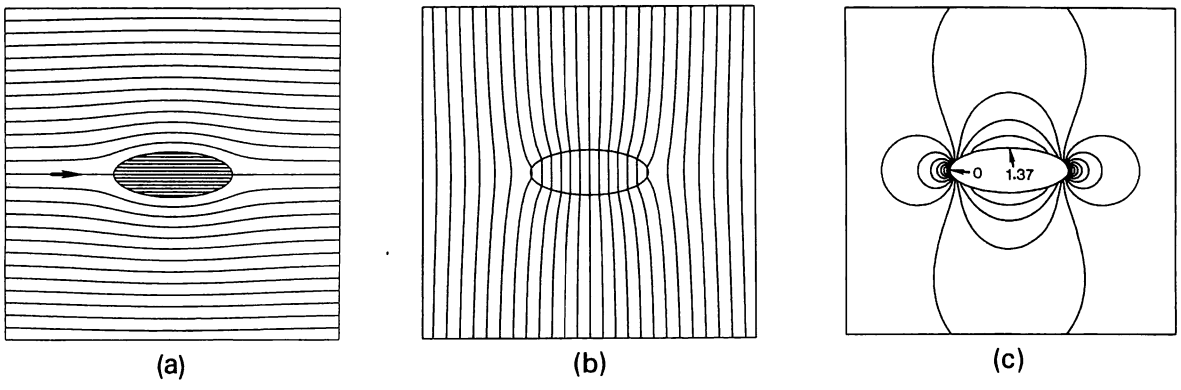

Fig. 3. Contours of flux function Ψ (a), potential Φ (b) and normalized current density $|j/j_0|$ (c) with an elliptical shape of the port (elongation ratio κ is 2.7) in the presence of constant electric field (arrow) in x direction (parallel to major axis).

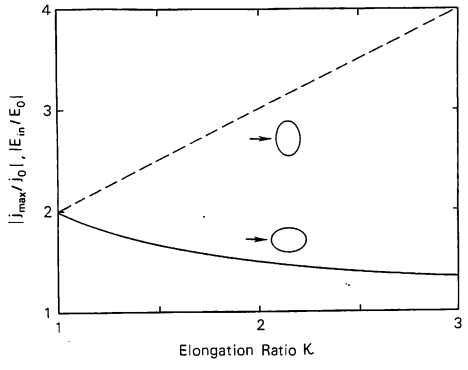

Fig. 4. Dependence of normalized maximum current density $|j_{max}/j_0|$ and electric field in the hole $|E_{in}/E_0|$ on elongation ratio κ of the port section in the presence of electric field in x direction. Here, $|j_{max}/j_0| = |E_{in}/E_0|$ is $1+\kappa$ (dashed line) and $=1+(1/\kappa)$ (solid line), respectively, for the case that major axes are perpendicular and parallel to x axis.

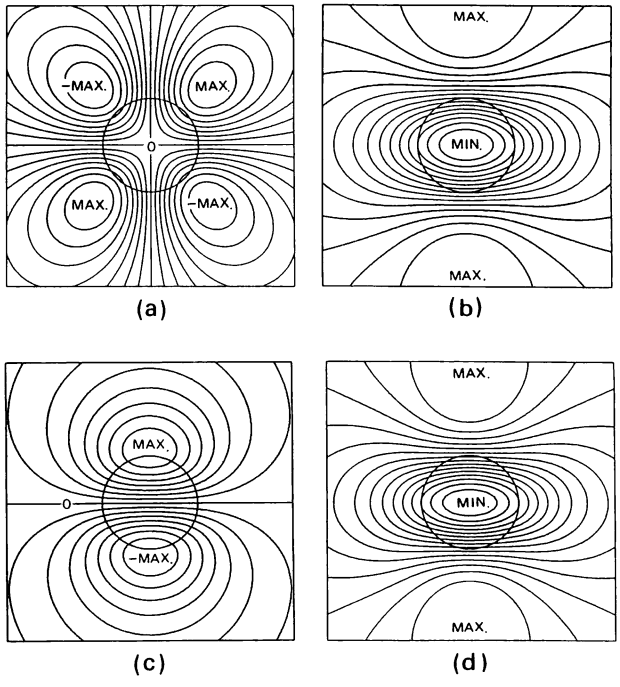

Fig. 5. Contours of B_x (a), B_y (b), B_z (c) and $|B|$ (d) on $z=1$ plane for the case of a circular port (see Fig. 1).

shown with constant electric fields in the x direction. With the increase in the elongation κ, both $|j_{max}/j_0|$ and $|E_{in}/E_0|$ (E_{in}: electric field in the hole region) increase rapidly as $1+\kappa$ when E_0 is parallel to the minor semiaxis, and decrease slowly as $1+(1/\kappa)$ when E_0 is parallel to the major semiaxis.

§4. Error Magnetic Field Distribution

Using the obtained liner current, the induced error magnetic fields are computed from the Biot Savart formula. Here, in this calculation, mesh sizes of the magnetic fields in both x and y directions are 70 for $|x|$, $|y| \leq 3$, while those of the liner current to calculate the magnetic fields are 80 for $|x|$, $|y| \leq 5$ and 100 for $5 < |x|$, $|y| \leq 100$. The error of this numerical calculation is within a few percent. Note that the error magnetic field profiles (length is normalized by the port size) and the maximum error field are not dependent on the port size, as can be seen from the Biot Savart formula.

Figure 5 shows the contours of the magnetic fields on the $z=1$ plane with a circular port for the same condition of Fig. 1. Here, the z axis is taken perpendicular to the (x, y) plane. The port hole is located on the $z=0$ plane with a radius of 1. From this, $|B_x|$ has the maximum near the port edge on $y=\pm x$, B_y has the maximum on $x=0$ and $y \approx 3$ and the minimum on $x=0$ and $y=0$, and $|B_z|$ has the maximum near the port edge on $x=0$. With the increase in the z direction, the value of y to have the maximum B_y increases rapidly, whereas the positions to have the maximum $|B_x|$ and $|B_z|$ depart from the port edge to the outer side slightly.

Figures 6 and 7 show the contours of the magnetic fields on the $z=1$ plane with an elliptical port for the same conditions of Figs. 2 and 3, respectively. The port hole is located on the $z=0$ plane with an elongation ratio of 2.7 (minor and major semiaxis lengths are 0.4 and 1.08, respectively). Similar results with the circular port are found.

The e-folding length of the magnetic fields in the z direction is considered. Figure 8 shows the relation between the magnetic fields and the position Z^* in the z direction with a circular port for the same condition of Fig. 1. Here, the Z^* is normalized with the length of a port radius, and j_0 is taken as 1 A/m. The important er-

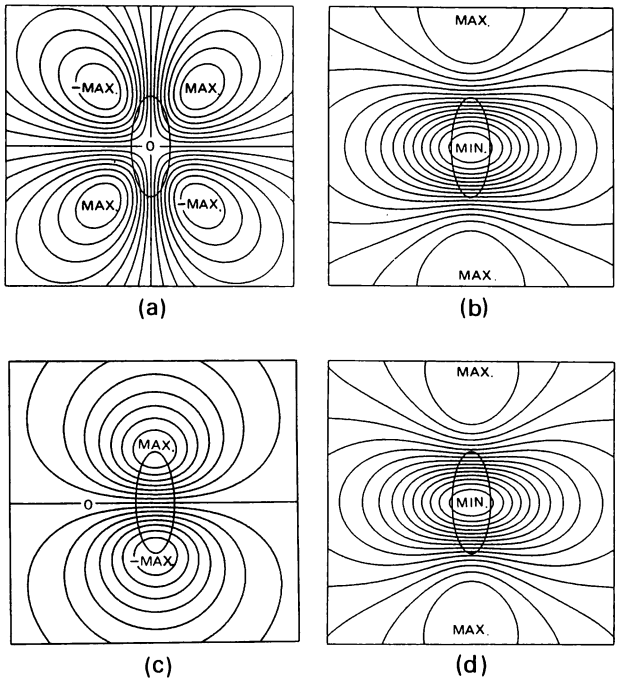

Fig. 6. Contours of B_x (a), B_y (b), B_z (c) and $|B|$ (d) on $z=1$ plane for the case of an elliptical port (see Fig. 2).

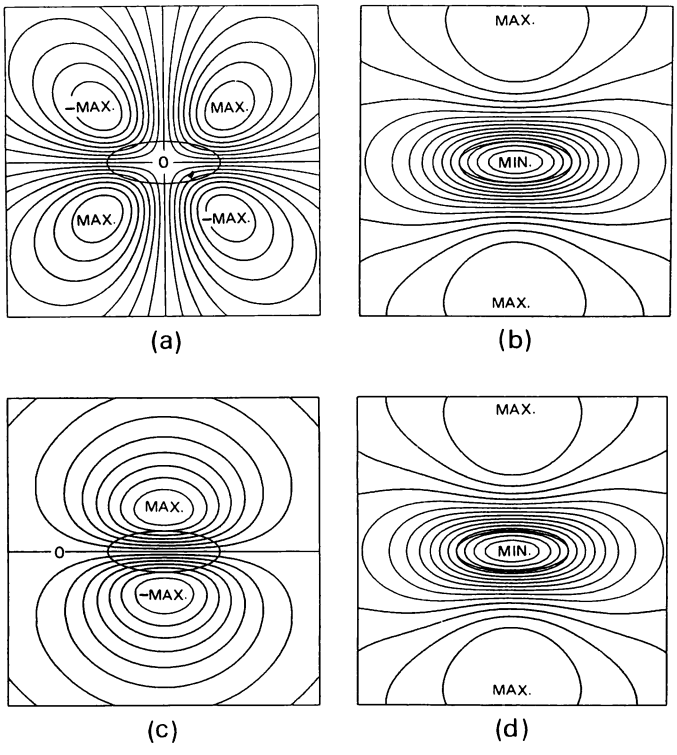

Fig. 7. Contours of B_x (a), B_y (b), B_z (c) and $|B|$ (d) on $z=1$ plane for the case of an elliptical port (see Fig. 3).

ror field considered experimentally is the B_z field, which is equivalent to the radial field for the cylindrical geometry. Near the port, $|B_z|$ has the maximum of about 10^{-2} Gauss and the e-folding length is about 0.3.

Without a port hole, $|B_y|$ has a constant value of $B_{y0}=\mu_0 j_0/2$ for the flat plane case regardless of the position, while, for the cylindrical case without a hole, B_y (poloidal field) is zero within the cylinder when the sur-

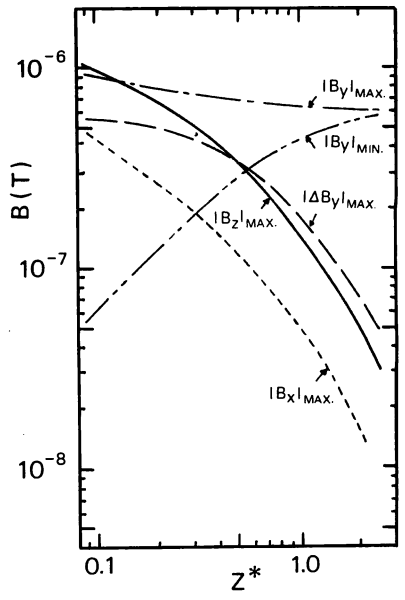

Fig. 8. Relation between magnetic fields and normalized position Z^* in z direction with a circular shape of the port (see Fig. 1).

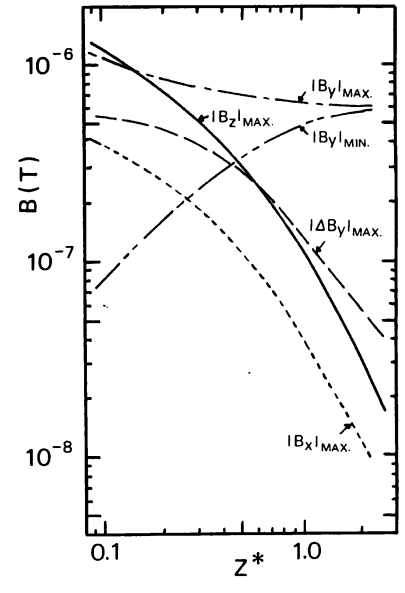

Fig. 9. Relation between magnetic fields and normalized position Z^* in z direction with an elliptical shape of the port (see Fig. 2).

face current flows along the central axis. Therefore, $\Delta B_y=B_y-B_{y0}$ corresponds to the poloidal field error by the port hole. Figure 8 shows that ΔB_y has the maximum near the port (about a half of the maximum $|B_z|$ value) and B_y approaches $\mu_0 j_0/2$ as Z^* increases.

In Fig. 9, the relation between the magnetic fields and the position Z^* in the z direction is shown for the same condition of Fig. 2 with an elliptical port. Here, the Z^* is also normalized with the length of a major semiaxis, and j_0 is taken as 1 A/m. The same trend with the circular port is found; the absolute values of B_z near the port and the e-folding length of B_z are larger and smaller by about 20%, respectively, than those with the circular port. When the current flows along the major axis (x direction) for an elliptical port, the induced error fields are smaller, as is shown in Fig. 10 (the same condition of Fig. 3); the

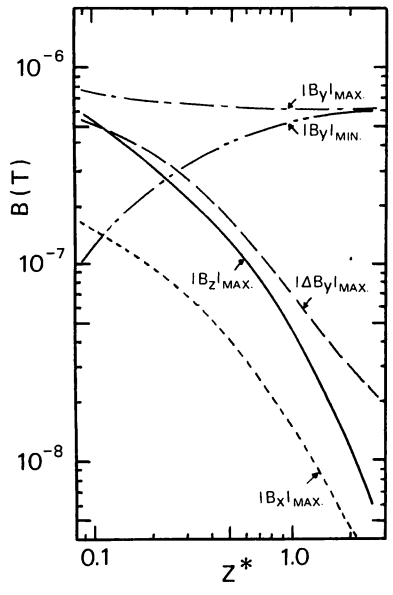

Fig. 10. Relation between magnetic fields and normalized position Z^* in z direction with an elliptical shape of the port (see Fig. 3).

B_z value is reduced to about half of it for the elliptical port with the current flowing along the minor axis (x direction), and the e-folding length normalized by the major semi axis length of ≈ 0.25.

Now we apply the numerical results to the REPUTE-1 device.[7,10,11] For the case that the plasma current $I_p = 200$ kA and loop voltage $V_l = 150$ V, j_0 becomes 17 kA/m as the toroidal resistance of the liner (minor radius is 22 cm) is 6.5 mΩ. Then, B_z, i.e., the radial field B_r, is estimated to be 180 Gauss near the port, which is 10% of the poloidal field generated by the plasma current. In order to reduce the error field, an increase in the liner resistance and a decrease in the plasma resistance are necessary. Reducing the port size does not decrease the maximum error field near the port as has been described before, although the region having the large error field is reduced.

§5. Conclusion

The liner current and electric field distributions near the port with the circular and elliptical cross sections are solved analytically by plane geometry from the analogy of the fluid mechanics. The value of $|j/j_0|$ becomes the maximum of $1+\kappa$ and $1+(1/\kappa)$ near the tips of the major and minor semiaxes, respectively, which are perpendicular to the applied electric field, and zero at the tips of the other semiaxes. Inside the hole, the constant electric fields normalized by E_0 are $1+\kappa$ and $1+(1/\kappa)$ when the major axes are perpendicular and parallel to the x axis, respectively. The disturbance in the current density distribution extends to about one port size in both x and y directions.

Using the Biot Savart formula, the induced (error) magnetic field profiles are derived from the analytic solution of the liner current distribution. The dominant error field is the B_z component, which has the maximum value near the point of the maximum current density (port edge). The e-folding length, taken along the axis (z direction) perpendicular to the plane, of B_z is about 0.25–0.3 normalized by a characteristic radius of the port. However, the maximum value does not change with the port size as long as the current density j_0 is not changed.

References

1) H. A. B. Bodin and A. A. Newton: Nucl. Fusion **20** (1980) 1255.
2) T. Tamano, W. D. Bard, T. N. Carlstrom, C. Chu, B. Curwen, R. K. Fisher, D. W. Graumann, R. R. Goforth, G. L. Jackson, R. J. LaHaye, T. Ohkawa, M. J. Schaffer, M. T. Saito, P. L. Taylor, T. S. Taylor, D. F. Register, S. E. Walker: *Proc. 10th Int. Conf. London, 1984* (Plasma Physics and Controlled Nuclear Fusion Research, 1984) (IAEA, Vienna, 1985) Vol. 2, p. 431.
3) D. A. Baker, C. J. Buchenauer, L. C. Burkhardt, E. J. Caramana, J. N. DiMarco, J. N. Downing, R. M. Erickson, R. F. Gribble, A. Haberstich, R. B. Howell, J. C. Ingraham, A. R. Jacobson, K. A. Klare, E. M. Little, R. S. Massey, J. G. Melton, G. Miller, R. W. Moses, C. P. Munson, J. A. Phillips, M. M. Pickrell, R. A. Nebel, A. E. Schofield, K. F. Schoenberg, R. G. Watt, P. G. Weber, D. M. Weldon, K. A. Werley, R. W. Wilkins, G. A. Wurden, D. D. Schnack, D. C. Baxter, A. Y. Aydemir, D. C. Barnes: *Proc. 10th Int. Conf. London, 1984* (Plasma Physics and Controlled Nuclear Fusion Research, 1984) (IAEA, Vienna, 1985) Vol. 2, p. 439.
4) P. G. Carolan, B. Alper, M. K. Bevir, H. A. B. Bodin, C. A. Bunting, D. R. Brotherton-Ratcliffe, H. Ahmed. D. E. Evans, D. Evans, A. R. Field, L. Firth, M. J. Forrest, C. G. Gimblett, N. C. Hawkes. I. H. Hutchinson, M Malacarne, A. Manley, A. A. Newton, P. G. Noonan, A. Patel, N. J. Peacock, D. P. Storey, H. Tsui, P. D. Wilcock: *Proc. 10th Int. Conf. London 1984* (Plasma Physics and Controlled Nuclear Fusion Research, 1984) (IAEA, Vienna, 1985) Vol. 2, p. 449.
5) Y. Hirano, Y. Kondoh, Y. Maejima, Y. Nogi, K. Ogawa, M. Sato, T. Shimada, Y. Yagi, H. Yoshimura: *Proc. 10th Int. Conf. London, 1984* (Plasma Physics and Controlled Nuclear Fusion Research, 1984) (IAEA, Vienna, 1985) Vol. 2, p. 475.
6) V. Antoni, M. Bassan, A. Buffa, S. Costa, L. Giudicotti, W. Grossmann, S. Martini, S. Ortolani, R. Paccagnella, M. E. Puiatti, P. Scarin, M. Valisa, E. Zilli: *Proc. 10th Int. Conf. London, 1984* (Plasma Physics and Controlled Nuclear Fusion Research, 1984) (IAEA, Vienna, 1985) Vol. 2, p. 487.
7) N. Asakura, T. Fujita, K. Hattori, N. Inoue, S. Ishida, Y. Kamada, S. Matsuzuka, K. Miyamoto, J. Morikawa, Y. Nagayama, H. Nihei, S. Shinohara, H. Toyama, Y. Ueda, K. Yamagishi, Z. Yoshida: Plasma Phys. & Controlled Fusion **28** (1986) 805.
8) K. I. Sato, T. Amano, Z. X. Chen, H. Arimoto, S. Yamada, A. Nagata, K. Yokoyama, Y. Kamada, A. Matsuoka, S. Masamune, H. Shindo, K. Saito, H. Murata, H. Oshiyama, S. Shiina, T. Tamaru: *Proc. 11th Int. Conf. Kyoto, 1986* (Plasma Physics and Controlled Nuclear Fusion Research, 1986) (IAEA, Vienna, 1987) Vol. 2, p. 413.
9) B. Alper, V. Antoni, M. K. Bevir, H. A. B. Bodin, C. A. Bunting, P. G. Carolan, J. Cunnane, D. E. Evans, A. R. Field, S. J. Gee, C. G. Gimblett, R. Hayden, T. R. Jarboe, P. Kirby, A. Manley, A. A. Newton, P. G. Noonan, A. Patel, R. S. Pease, M. G. Rusbridge, K. P. Schneider, D. P. Storey, H. Y. W. Tsui, S. Whitfield, P. D. Wilcock: *Proc. 11th Int. Conf. Kyoto, 1986* (Plasma Physics and Controlled Nuclear Fusion Research, 1986) (IAEA, Vienna, 1987) Vol. 2, p. 399.
10) Z. Yoshida, N. Inoue, H. Yamada, S. Hamaguchi, K. Itami, N. Suzuki, K. Hattori, Y. Kamada, K. Okano, J. Morikawa, H. Nihei, K. Miyamoto, T. Uchida, T. Sato: *Proc. 10th Int. Conf. London, 1984* (Plasma Physics and Controlled Nuclear Fusion Research, 1984) (IAEA, Vienna, 1985) Vol. 2, p. 467.
11) N. Asakura, A. Fujisawa, T. Fujita, Y. Fukuda, K. Hattori, N. Inoue, S. Ishida, K. Itami, Y. Iwata, H. Ji, Y. Kamada, K. Kusano, S. Matsuzuka, K. Miyamoto, J. Morikawa, C. Munson, Y. Murakami, Y. Nagayama, H. Nihei, S. Onodera, M. Saito, T. Sato, S. Shinohara, H. Toyama, Y. Ueda, M. Utumi, H. Yamada, K. Yamagishi, Z. Yoshida: *Proc. 11th Int. Conf. Kyoto, 1986* (Plasma Physics and Controlled Nuclear Fusion Research, 1986) (IAEA, Vienna, 1987) Vol. 2, p. 433.